Macroscopic Objects | Hot Paper

DOI: 10.1002/ange.201402827

Cooperative, Reversible Self-Assembly of Covalently Pre-Linked Proteins into Giant Fibrous Structures**

Saadyah Averick, Orsolya Karácsony, Jacob Mohin, Xin Yong, Nicholas M. Moellers, Bradley F. Woodman, Weipu Zhu, Ryan A. Mehl, Anna C. Balazs, Tomasz Kowalewski,* and Krzysztof Matyjaszewski**

Dedicated to Professor George M. Whitesides on the occasion of his 75th birthday

Abstract: *We demonstrate a simple bioconjugate polymer system that undergoes reversible self-assembling into extended fibrous structures, reminiscent of those observed in living systems. It is comprised of green fluorescent protein (GFP) molecules linked into linear oligomeric strands through click step growth polymerization with dialkyne poly(ethylene oxide) (PEO). Confocal microscopy, atomic force microscopy, and dynamic light scattering revealed that such strands form high persistence length fibers, with lengths reaching tens of micrometers, and uniform, sub-100 nm widths. We ascribe this remarkable and robust form of self-assembly to the cooperativity arising from the known tendency of GFP molecules to dimerize through localized hydrophobic patches and from their covalent pre-linking with flexible PEO. Dissipative particle dynamics simulations of a coarse-grained model of the system revealed its tendency to form elongated fibrous aggregates, suggesting the general nature of this mode of self-assembly.*

Reversible self-assembly of biological macromolecules into fibrous structures through hydrogen bonding and/or hydrophobic interactions plays a significant role in many biological processes.[1] Prominent examples of such structures include collagen fibers, which are a key component of extracellular matrix, and actin filaments, which form the scaffolds of cytoskeleton.[2] Dynamic assembly and disassembly of actin filaments is driven by enzymatic catalysis and facilitates essential dynamic cellular processes such as cell division and growth. Inhibition of actin disassembly is one of the primary targets of anti-cancer drugs such as monomethyl auristatin E and paclitaxel.[3] Systems utilizing reversible fibrous self-assembly are actively sought for applications such as tissue engineering, drug delivery, nanoreactors and imaging.[4] One of the prime examples of recently developed synthetic biomaterials that utilize such a process are functional scaffolds formed by precisely engineered protein/peptide-amphiphiles.[5]

Herein, we demonstrate a novel robust path to the reversible self-assembly of fibrous structures that utilizes oligomeric strands comprised of compactly-folded protein molecules connected by flexible linkers as the primary building blocks. The discovery of this path was serendipitous, and stems from our earlier work on the modification of green fluorescent protein (GFP) for the purpose of bioconjugation. In the present work, all GFP molecules were functionalized with a pair of specifically placed azide groups (amino acid resides 134 and 150), and then linked together through a click reaction[6] with dialkyne terminated poly(ethylene oxide) (PEO) linkers. In polymer chemistry, this scheme of linking difunctional species is referred to as a step-growth polymerization. One of the hallmarks of the step-growth is that, in contrast with the chain growth, species ranging from small oligomers to high degree of polymerization products coexist throughout the entire process. Indeed, in our past work with such click step growth processes, we have observed primarily low degree of polymerization products[7] and some cyclized species.[7a,8] Surprisingly, the oligomeric products of our current GFP linking reaction prepared via click-driven step growth formed giant fibrous objects readily visualized by fluorescence confocal microscopy. The unlikely possibility that those objects represented ultra-high degree of polymerization covalently linked strands was ruled out by further observations that the fibers could be disrupted by sonication and then would spontaneously reform. This led us to hypothesize that the reversible assembly of giant fibers was driven by the well-established tendency of GFP molecules to

[*] S. Averick, O. Karácsony,[+] J. Mohin,[+] Prof. T. Kowalewski, Prof. K. Matyjaszewski
Department of Chemistry, Carnegie Mellon University
4400 Fifth Ave, Pittsburgh, PA 15213 (USA)
E-mail: tomek@andrew.cmu.edu
km3b@andrew.cmu.edu
Dr. X. Yong, N. M. Moellers, Prof. A. C. Balazs
Chemical Engineering Department, University of Pittsburgh
Pittsburgh, PA 15213 (USA)
E-mail: balazs@pitt.edu
B. F. Woodman, Prof. R. A. Mehl
Department of Biochemistry and Biophysics
Oregon State University
Corvallis, OR 97331 (USA)
Prof. W. Zhu
MOE Key Laboratory of Macromolecular Synthesis and Functionalization, Department of Polymer Science and Engineering
Zhejiang University, Hangzhou 310027 (P.R. China)
[+] These authors contributed equally to this work.

[**] We thank the CRP Consortium, the NSF (DMR 09-69301, NSF-MCB-0448297), and the Oregon State University (grant number P30 ES00210) for funding. A.C.B. and K.M. gratefully acknowledge financial support from the DOE.

Supporting information for this article is available on the WWW under http://dx.doi.org/10.1002/anie.201402827.

aggregate into dimers through the hydrophobic interaction between the localized surface patches of non-polar residues.

Self-assembly through the interaction of hydrophobic patches is common in biological systems. One of its most prominent examples is the formation of transmembrane pores by porins.[9] Porins are beta barrel proteins that encompass distinct hydrophobic and hydrophilic faces on their surfaces. Given this surface amphipathicity, porins assemble into channels in lipid membranes, with hydrophobic sides facing the nonpolar membrane environment and hydrophilic sides lining the interior of the channel. When the hydrophobic surface patches are more localized, such that they become covered when two protein molecules come into contact, the aggregation becomes limited to dimerization, as in the case of green fluorescent protein GFP, which is also a beta barrel protein.[10] In the remainder of this report, we provide a detailed description of the synthesis and characterization of GFP–PEO assemblies, and demonstrate the plausibility of the proposed fiber formation mechanism through computer simulations of the self-assembly process.

The localized hydrophobic patches, which drive the dimerization of GFP, are comprised of Ala^{206}, Leu^{221}, and Phe^{223} localized on the protein surface. The reactive azide moieties were attached to the GFP surface by site-directed mutagenesis, in the locations away from the hydrophobic patch (see Scheme S1 in the Supporting Information (SI)). As shown in Scheme 1, such difunctionalized protein (GFP-diN_3)

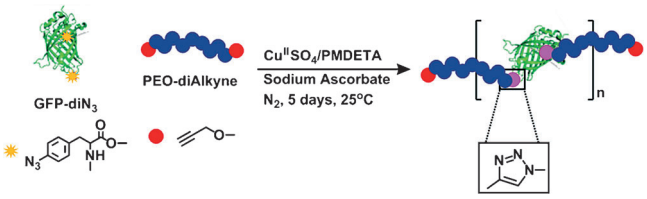

Scheme 1. Fiber synthesis: Click step-growth polymerization approach was used for preparing GFP–PEO fibers. Synthetic conditions: GFP-diN_3: 0.7 μmol, PEO-dialkyne: 0.7 μmol, PMDETA: 9.1 μmol, $CuSO_4 \cdot 5\,H_2O$: 7 μmol, sodium ascorbate: 7.7 μmol, in 1× PBS. PMDETA = Pentamethyldiethylenetriamine.

molecules were then directly copolymerized with DP = 20 monodiperse dialkyne terminated poly(ethylene oxide) (PEO-dialkyne) under mild aqueous reaction conditions using click chemistry in the presence of Cu^{I} catalyst generated by the reduction of Cu^{II} with sodium ascorbate.[6a,c,11] Formation of oligomeric species was confirmed using denaturing gel electrophoresis (SI, Figure S1). The first indication that assembly of fibers occurred was gleaned from dynamic light scattering (DLS). Solutions of the reaction mixture were pelleted, using centrifugation and suspended in 1× PBS (phosphate-buffered saline) at a concentration of 0.1 mg mL^{-1}. The size distribution of the GFP–PEO aggregates determined using DLS and shown in Figure 1 A (bold line "before sonication") pointed to the presence of relatively well-defined species with a hydrodynamic diameter of approximately 430 ± 50 nm. In contrast, DLS analysis of a control sample, where the sodium ascorbate was not added

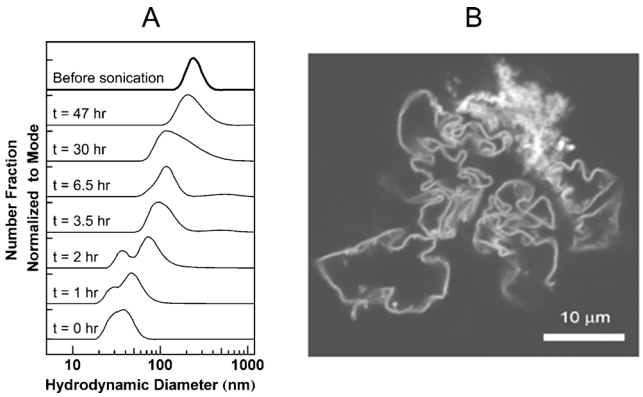

Figure 1. A) DLS size distribution of GFP–PEO aggregates normalized to their modes and shifted vertically for clarity. The top trace shows the distribution for an aged suspension of fibers. Traces below demonstrate re-assembly of fibers following their disruption by sonication. B) Confocal fluorescence microscopy image of a giant fibrous aggregate of GFP–PEO deposited on glass by drop-casting of 1 μg mL^{-1} solution. For a color version please see the Supporting Information.

to the reaction mixture and no click chain extension occurred, revealed only ca. 5 nm particles (SI, Figure S2). The latter size matches that of native GFP and confirms that, indeed, a click-mediated step-growth polymerization/oligomerization occurred after the addition of the reducing agent. To demonstrate that the observed aggregates were formed by protein specific interaction we treated the purified reaction mixture with trypsin, a protease, for four days and found that the mean diameter of the particles in solution decreased to ca. 10 nm, indicating the successful enzymatic degradation (SI, Figure S3).

After polymerization and aggregation, the suspensions remained fluorescent, indicating that mild conditions used in the step growth allowed the GFP molecules to retain their tertiary structure. Confocal fluorescence microscopy images of the samples deposited on glass by drop-casting from solution revealed the presence of giant fibrous aggregates of uniform width and persistence length exceeding locally several μm (Figure 1 B).

The ability of the fibers to reversibly disassemble and assemble was studied using DLS. The fiber disassembly was evident from the DLS of the solution that was subjected to ultrasonication for 180 s, with a one-second interval (Figure 1 A). As shown in Figure 1 A, subsequent DLS monitoring of the solution revealed that the aggregates reformed after 40 h, demonstrating the reversibility of this assembly.

Sub-μm morphology of fibers was studied using tapping mode atomic force microscopy (AFM). The samples were prepared by deposition of aqueous protein solutions (1 μg mL^{-1} fiber, 2 nM $CaCl_2$) onto two kinds of atomically flat surfaces routinely used in AFM imaging of biological molecules: hydrophilic freshly cleaved mica and hydrophobic freshly cleaved highly ordered pyrolytic graphite (HOPG). The deposition protocol involved flowing of 30 μL aliquots over sharply tilted substrates, with the excess solution shaken-off after 10–30 s, followed by quick drying with a jet stream of compressed nitrogen. In all cases, AFM images of such

prepared samples revealed the presence of distinct nanostructures and were free of ill-defined particulates. HOPG was ultimately selected as a substrate for the majority of experiments, owing to the ease with which the areas to be imaged could be identified using optical video microscopy.

When aged solutions were used, inspection of the HOPG surface revealed the presence of sparsely distributed giant fibrous structures with lengths on the order of tens of μm, reminiscent of those observed by confocal microscopy. As shown in the image taken across one of such fibers (Figure 2

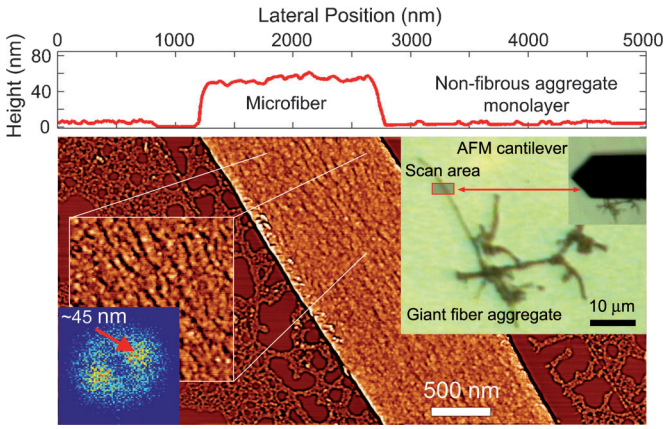

Figure 2. Tapping mode AFM height image of the giant fibrous aggregate of GFP–PEO hybrids surrounded by non-fibrous species deposited on the surface of HOPG from aged aqueous solution. In order to facilitate visualization of fine features, the image has been digitally processed by applying a custom isotropic soft-edge band-pass filter. Comparison with unprocessed height, phase and amplitude images (see Supporting Information) confirmed that processing did not introduce any artifacts and faithfully revealed the details of nanoscale surface topography. Top: Cross-sectional height profile across the unfiltered image illustrates the height difference between the fibrous aggregate, and non-fibrous species, the height of which (ca. 5 nm) is comparable with the size of GFP molecules. Top-right inset: Image from the optical video microscope used to position the AFM tip over the giant aggregate. Red rectangle indicates the scan area. Bottom-left inset: Zoomed-in portion of the fiber surface showing the characteristic quasi-periodic nanofibrous substructure, and the 2-D power spectrum of Fourier transform of this portion of the image. The distinct anisotropic lobes in the Fourier transform reflect the orientation of nanofibers along the fiber axis and their positions provide the average lateral spacing (ca. 45 nm).

and SI, Figure S6), the fiber deposited on the surface had a distinct flattened appearance, which was also observed to a various degrees in the images of other fibers (SI, FigureS S4 and S5). It should be pointed out that this flat shape does not necessarily need to reflect the native structure of the fibers, since they could have undergone partial lateral collapse upon adsorption. Of particular interest in the image shown in Figure 2 is the characteristic nanoscale texture of the fiber, which is highly suggestive of the nanofibrous substructure running along the fiber axis. High degree of directionality and lateral periodicity (ca. 46 nm) of this substructure is evident in the power spectrum of the 2-D Fourier transform of the image (inset at the bottom left). Inspection of the area surrounding the fiber reveals the presence of a distinct lace-like layer of uniform thickness of ca. 3 nm comprised of uniform globular features, which can be ascribed to non-aggregated GFP molecules present on the surface. This assignment is further confirmed by the fact that similar uniform sub-monolayers of aggregates were consistently observed upon deposition of solutions aged for different amounts of time and were present in the control samples prepared from diazide-GFP conjugated to mono-alkyne GFP (SI, Figure S7).

In an attempt to identify the products forming at the early stages of aggregation the AFM samples were also prepared from freshly sonicated solutions. In this case, in addition to characteristic monolayers of GFP, the AFM images occasionally revealed the presence of highly uniform segmented nanofibers such as those shown in Figure 3 A and in SI, Figures S8 and S9. Quantitative size analysis of those nanofibers (Figure 4 B–F) revealed that their height, apparent width, and average domain spacing along the backbone did not exceed the average size of, respectively, single, ca. 7 and ca. 10 GFP molecules. These feature sizes indicate that the observed nanofibers represent the earliest, protofibrillar stage of aggregation. They are also comparable with the feature sizes within characteristic unidirectional substructure of the giant fibers described above, suggesting that protofibrillar species comprise the basic building block of those fibers.

To gain insight into the self-assembly process and analyze the microscopic structure of the protein–polymer complexes, we conducted simulations using dissipative particle dynamics (DPD), which can be viewed as a coarse-grained molecular dynamics (MD) method.[12] In our simulation, each GFP particle is modeled as a barrel-shaped cluster of hydrophilic DPD beads arranged in an FCC lattice structure (Figure 4). The beads are connected by harmonic spring-like bonds.[13] A row of four hydrophobic beads on the face of each GFP barrel represents the hydrophobic patch as shown in Scheme 1. The PEO chains linking the GFP particles are modeled by a sequence of N_l DPD beads, where adjacent beads are connected by the harmonic spring-like bonds.[14] We performed simulations with different PEO chain lengths $N_l = 10$, 20 or 30, corresponding to different degrees of polymerization. These PEO chains are attached to two beads on the surface of the GFP, whose positions are chosen to approximately represent the modified amino acid sites at positions 134 and 150 (SI, Scheme S1).

We refer to the PEO-linked GFP particles as a strand. Because the step-growth polymerization produces strands with a wide range of molecular weights, we modeled a disperse system in which strands have different numbers of GFP units. Here, a strand of length three has three GFP units linked by three PEO chains (see Figure 4). Our simulations encompass strands of lengths three, four or five. We simulated systems with two densities of PEO–GFP complexes; the $N_c = 3$ system contains three strands with a total of 12 GFP units and 12 PEO chains as linkers. (The three strands have length three, four and five.) The $N_c = 6$ system doubles the density of the PEO–GFP complexes by having total 24 GFP and 24 PEO chains in the same simulation box. In the latter system, there are two strands for each length. The GFP strands are immersed in a hydrophilic solution, which fills the

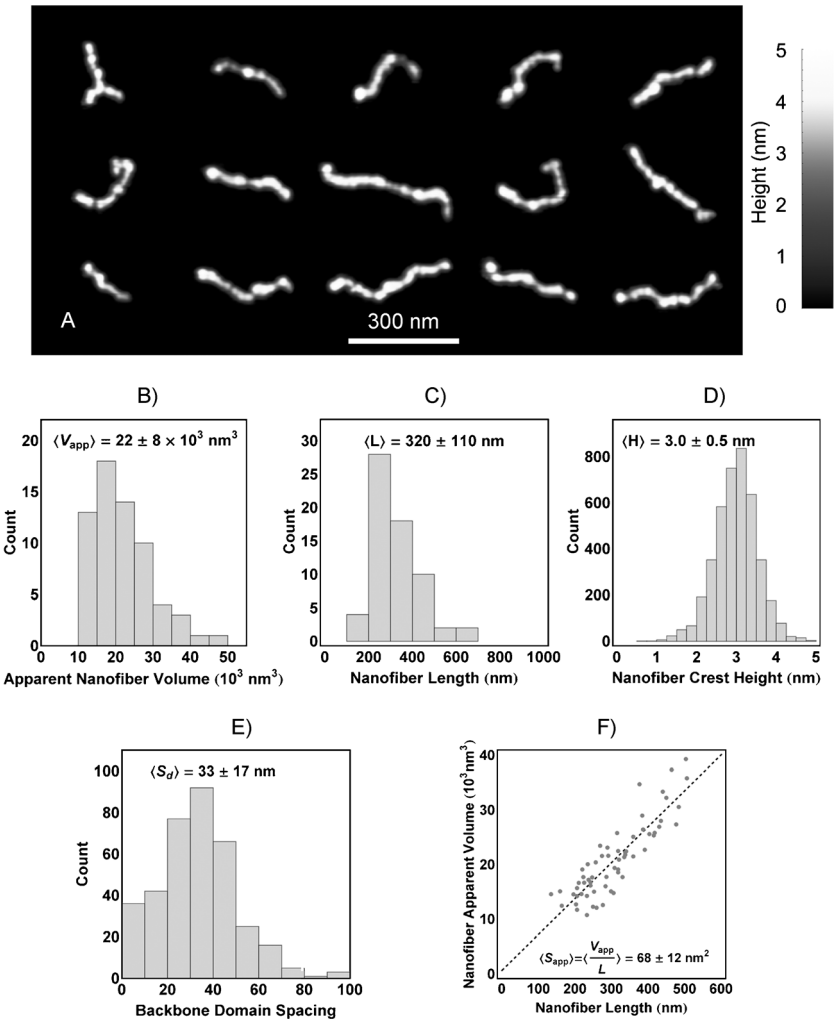

Figure 3. A) Gallery of tapping mode AFM height image of nanofibrous aggregates deposited on HOPG within 2 h after ultra-sonication aimed at disassembly of giant fibers. Images of individual nanofibers were manually selected from a 5 μm × 5 μm image (SI, Figure S7). Panels (B)–(E) show the results of quantitative size analysis of individual nanofibers which was performed on individual sub-images previously subjected to first order line-by-line baseline subtraction. Corrected sub-images were then binarized and the individual nano-objects were detected and analyzed using standard morphological imaging procedures. The histogram plot in (B) shows the distribution of apparent volumes of individual nanofibers which were determined by 2-D numerical integration. The distribution of lengths (C) is based on the contour lengths of binarized image skeletons calculated by digital thinning. The distribution of heights (D) is based on the heights extracted from the images at the points corresponding to the crests of nanofibers. The heights are narrowly distributed around 3 nm, which is close to the average dimension of a single GFP molecule. The distribution of backbone domain spacings (E) is based on the distances between the maxima on the nanofiber crest profiles. The linear correlation between the apparent volumes and lengths of nanofibers (F) reflects their uniform widths. The apparent lateral cross-section of the fibers obtained from this correlation was equal to ca. 70 nm^2 (cf. ca. 10 nm^2 for the average projected area of individual GFP molecule). For a color version please see the Supporting Information.

remaining volume of the simulation box and gives a total bead density of $\rho = 3$. The hydrophobic interactions are captured by specifying the repulsive interactions a between the beads. We set the repulsion parameter for any two beads of the same type to $a_{ii} = 25\ k_B T$.[12b] The value of the repulsion parameter between the hydrophobic-hydrophilic moieties is specified as $a_{ij} = 100\ k_B T$.[13] (These values lead to the formation of stable dimers in a system containing only GFP particles.) During the first 2×10^5 time steps, we turn off the hydrophobic interactions to achieve a random dispersion of GFP strands. The hydrophobic interactions are then turned on and the simulations are run for an additional 2×10^6 time steps to allow the system to attain thermodynamic equilibrium.

To quantify the formation of aggregates, for each simulation time frame, coordinates of constituent beads were transformed from the laboratory frame (x_L, y_L, z_L) to the principal components coordinate system (x,y,z) as shown in SI, Figure S10 A,B.

The transformation procedure involved shifting all the coordinates to the center of mass and computing the eigenvectors of their covariance matrix. Final transformed coordinates (x,y,z) were then computed as projections onto those eigenvectors. As a result of such transformations, the directions of largest, medium and smallest variances of bead positions became aligned, respectively, along the x, y and z axes with $\sigma_x^2 > \sigma_y^2 > \sigma_z^2$ as shown by the positioning of the "2σ ellipsoid" and its projections on the xy, xz and zy planes shown in Figure 6. For the purpose of further quantitative analysis, the aggregates were coarsened by calculating the discrete distribution of bead center coordinates using $1 \times 1 \times 1$ cubic bins (voxels). The resulting smoothed 3D surface contour plot of such a coarsened aggregate is shown in SI, Figure S10 C. In addition, binary 2D projections of aggregates onto the xy, xz and yz planes were calculated by summing the 3D distributions, respectively, along the z, y and x directions and thresholding the resulting 2D images by setting all non-zero pixel values to unity (SI, Figure S10 C). The overall shape anisotropy of the aggregates was described by their aspect ratio $\eta = \sigma_x \sigma_y \sigma_z =$ $^{-1/2}$, whereas their effective spanning volume was computed as $\nu = (4/3)\pi$-$(\sigma_x \sigma_y \sigma_z)$.

The evidence for the aggregation of the strands into single contiguous objects came from the analysis of the number of coarsened objects within each simulation frame as a function of time steps (SI, Figures S11 and S12). In all instances, as soon as the hydrophobic interaction was turned on, the number of objects within each frame sharply decreased and tended in a fluctuating fashion to unity. Inspection of the evolution of the number of coarsened objects with time for all simulation runs (SI, Figure S12) indicated that coalescence of strands into a single object was

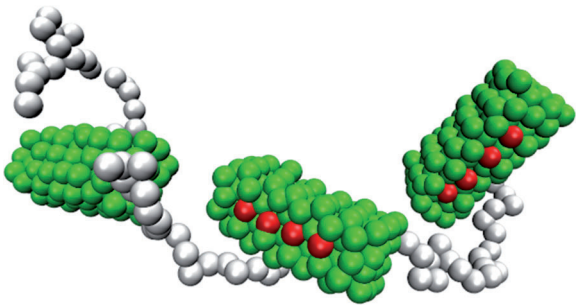

Figure 4. PEO-linked GFP strands with 3 GFP units. Green and red beads are hydrophilic and hydrophobic GFP beads, respectively. White beads represent PEO units.

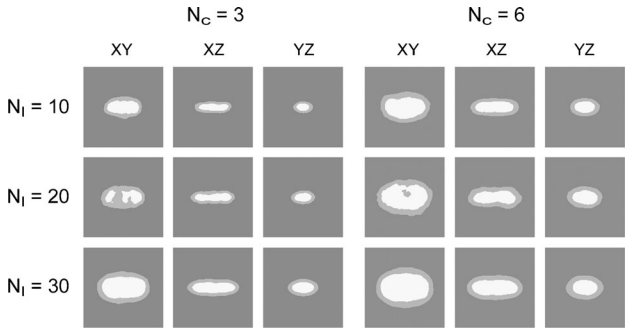

Figure 6. Average *xy*, *xz* and *yz* projections of single objects taken over all simulation runs under different conditions. For a color version please see the Supporting Information.

more robust for assemblies comprised of 6 strands. As shown in SI, Figure S11 B, the formation of single objects appeared to be weakly favoured by longer linker lengths, with the trend being more pronounced for the 3-strand assemblies. Overall, the aggregates tended to adopt the elongated shape, which was reflected by the increase of their aspect ratio with the decrease of effective spanning volume (SI, Figures 13 and 14). The selection of 2D *xy* projections of single-object aggregates viewed in the principal component coordinate that most clearly revealed their fibrous character is presented in Figure 5.

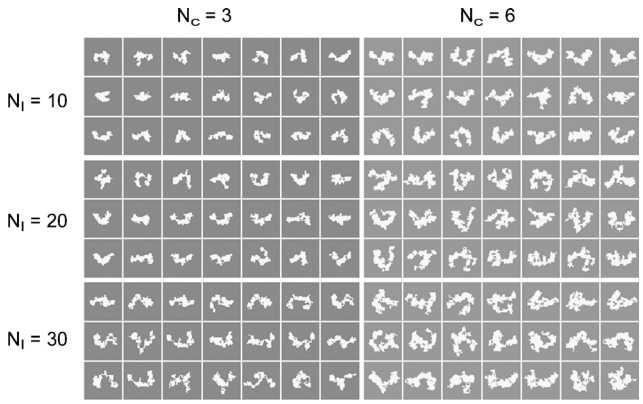

Figure 5. Gallery of *xy* plane projections of fibrous species observed for different simulation conditions (SI, Figure S11). For a color version please see the Supporting Information.

Beyond these unambiguously fibrous shapes, the shapes of 2D *xy* projections of single-object aggregates fluctuated broadly, as shown in the complete galleries of projections included in Supporting Information. Nevertheless, the 2D projections averaged over all single-object aggregates transformed into the principal component coordinate system shown in Figure 6 pointed to their overall elongated character. This was particularly apparent from the markedly elongated shape of projections of aggregates onto the *xz* plane and from their compact projections onto the *yz* plane. The apparently less marked elongation of the aggregates in the *xy* plane was caused by their high tendency to curve, evident clearly in the projections of individual fibers shown in Figure 5. Comparison of the overall aggregate projections for 3-strand and 6-strand assemblies (Figure 6 left versus right) indicates that, not surprisingly, the former adopted more slender shapes. Altogether, the above analysis indicates that our simulations indeed confirmed the fiber-forming tendency of the assemblies comprised of bulk dimerizing species connected by flexible linkers. Moreover, we believe that the nanofibrous assemblies revealed in the simulation closely correspond to the protofibrillar species observed in AFM imaging of samples deposited from freshly sonicated solutions.

In conclusion, we have demonstrated a novel GFP bioconjugate system capable of reversible formation of giant fibers, and presented the evidence and arguments that its self-assembly is driven by the hydrophobic dimerization of GFP molecules covalently linked with PEO chains into oligomeric strands. Our results point toward a simple method for preparing complex functional materials using discrete molecular interactions of oligomers. The apparent general nature of this self-assembly process implies that it could be readily utilized to fabricate new materials for drug delivery and tissue engineering applications.

Experimental Section

Amber codon suppression technology was employed to incorporate two unnatural amino acids (codon: UAA) containing azide functionality at surface-exposed residues (amino acid residues134 and 150) of GFP (Scheme 1). A *Methanococcus jannaschii* (Mj) tyrosyl-tRNA synthetase (RS)/tRNACUA pair was used for the co-translational and site-specific incorporation of *p*-azidophenylalanine (pN3F) into GFP. See SI for detailed protein expression and purification conditions.

The click step growth polymerization was conducted by dissolving PEO-dialkyne (See SI for synthesis of PEO-dialkyne), $CuSO_4{\cdot}5H_2O$, and PMDETA in water followed by dropwise addition of a solution containing GFP-diN3 in phosphate buffer saline (1 × PBS, pH 7.4). The reaction mixture was protected from light, and sodium ascorbate was added to produce Cu^I in situ. The reaction was stirred for 5 days, centrifuged, and the supernatant discarded. The GFP–PEO fibers were resuspended and centrifuged two additional times with PBS, to remove the catalyst and any unreacted GFP.

Received: February 26, 2014
Revised: May 9, 2014
Published online: July 9, 2014

Keywords: bioconjugation · click chemistry · dissipative particle dynamics · protein fibers · self-assembly

[1] a) P. A. Huijing, *J. Biomech. Eng.* **1999**, *32*, 329 – 345; b) T. D. Pollard, G. G. Borisy, *Cell* **2003**, *112*, 453 – 465; c) M. F. Carlier, S. Wiesner, C. Le Clainche, D. Pantaloni, *C. R. Biol.* **2003**, *326*, 161 – 170; d) C. Janke, J. C. Bulinski, *Nat. Rev. Mol. Cell Biol.* **2011**, *12*, 773 – 786.

[2] a) F. T. Bosman, I. Stamenkovic, *J. Pathol.* **2003**, *200*, 423 – 428; b) T. D. Pollard, J. A. Cooper, *Science* **2009**, *326*, 1208 – 1212.

[3] F. Pellegrini, D. R. Budman, *Cancer Invest.* **2005**, *23*, 264 – 273.

[4] a) I. W. Hamley, *Soft Matter* **2011**, *7*, 4122; b) H. Hosseinkhani, P.-D. Hong, D.-S. Yu, *Chem. Rev.* **2013**, *113*, 4837 – 4861; c) A. Lakshmanan, S. Zhang, C. A. E. Hauser, *Trends Biotechnol.* **2012**, *30*, 155 – 165; d) H. Cui, M. J. Webber, S. I. Stupp, *Biopolymers* **2010**, *94*, 1 – 18; e) C. J. Bowerman, B. L. Nilsson, *Biopolymers* **2012**, *98*, 169 – 184; f) D. M. Vriezema, M. Comellas Aragonès, J. A. A. W. Elemans, J. J. L. M. Cornelissen, A. E. Rowan, R. J. M. Nolte, *Chem. Rev.* **2005**, *105*, 1445 – 1490.

[5] a) Z. B. Li, T. J. Deming, *Soft Matter* **2010**, *6*, 2546 – 2551; b) V. Z. Sun, Z. B. Li, T. J. Deming, D. T. Kamei, *Biomacromolecules* **2011**, *12*, 10 – 13; c) A. R. Rodriguez, U.-J. Choe, D. T. Kamei, T. J. Deming, *Macromol. Biosci.* **2012**, *12*, 805 – 811; d) J. A. A. W. Elemans, A. E. Rowan, R. J. M. Nolte, *J. Mater. Chem.* **2003**, *13*, 2661.

[6] a) H. C. Kolb, M. G. Finn, K. B. Sharpless, *Angew. Chem.* **2001**, *113*, 2056 – 2075; *Angew. Chem. Int. Ed.* **2001**, *40*, 2004 – 2021; b) M. D. Best, *Biochemistry* **2009**, *48*, 6571 – 6584; c) P. L. Golas, K. Matyjaszewski, *Chem. Soc. Rev.* **2010**, *39*, 1338 – 1354.

[7] a) N. V. Tsarevsky, B. S. Sumerlin, K. Matyjaszewski, *Macromolecules* **2005**, *38*, 3558 – 3561; b) B. S. Sumerlin, N. V. Tsarevsky, G. Louche, R. Y. Lee, K. Matyjaszewski, *Macromolecules* **2005**, *38*, 7540 – 7545.

[8] B. A. Laurent, S. M. Grayson, *J. Am. Chem. Soc.* **2006**, *128*, 4238 – 4239.

[9] H. Nikaido, *Microbiol. Mol. Biol. Rev.* **2003**, *67*, 593 – 656.

[10] a) R. Y. Tsien, *Annu. Rev. Biochem.* **1998**, *67*, 509 – 544; b) S. J. Remington, *Protein Sci.* **2011**, *20*, 1509 – 1519.

[11] a) K. Nwe, M. W. Brechbiel, *Cancer Biother. Radiopharm.* **2009**, *24*, 289 – 302; b) W. Shi, S. Dolai, S. Averick, S. S. Fernando, J. A. Saltos, W. L′Amoreaux, P. Banerjee, K. Raja, *Bioconjugate Chem.* **2009**, *20*, 1595 – 1601; c) S. E. Averick, E. Paredes, D. Grahacharya, B. F. Woodman, S. J. Miyake-Stoner, R. A. Mehl, K. Matyjaszewski, S. R. Das, *Langmuir* **2012**, *28*, 1954 – 1958; d) J. L. Brennan, N. S. Hatzakis, T. R. Tshikhudo, V. Razumas, S. Patkar, J. Vind, A. Svendsen, R. J. M. Nolte, A. E. Rowan, M. Brust, *Bioconjugate Chem.* **2006**, *17*, 1373 – 1375.

[12] a) P. J. Hoogerbrugge, J. M. V. A. Koelman, *Europhys. Lett.* **1992**, *19*, 155 – 160; b) R. D. Groot, P. B. Warren, *J. Chem. Phys.* **1997**, *107*, 4423 – 4435.

[13] a) I. Salib, X. Yong, E. J. Crabb, N. M. Moellers, G. T. McFarlin, O. Kuksenok, A. C. Balazs, *ACS Nano* **2013**, *7*, 1224 – 1238; b) X. Yong, E. J. Crabb, N. M. Moellers, A. C. Balazs, *Langmuir* **2013**, *29*, 16066 – 16074.

[14] X. Yong, O. Kuksenok, K. Matyjaszewski, A. C. Balazs, *Nano Lett.* **2013**, *13*, 6269 – 6274.

